Research Square

Preprints are preliminary reports that have not undergone peer review.
They should not be considered conclusive, used to inform clinical practice,
or referenced by the media as validated information.

Angle-Based Star Occultation Measurements for Spacecraft Navigation

Jack A. Joshi

jack.a.joshi@my.utexas.edu

The University of Texas at Austin

Renato Zanetti

The University of Texas at Austin

Ryan P. Russell

The University of Texas at Austin

Research Article

Keywords: Star occultation, elevation angle, star tracker, cislunar space

Posted Date: November 20th, 2026

DOI: https://doi.org/10.21203/rs.3.rs-11485647/v1

License: This work is licensed under a Creative Commons Attribution 4.0 International License.
Read Full License

Additional Declarations: No competing interests reported.

Angle-Based Star Occultation Measurements for Spacecraft Navigation

Jack A Joshi[1*], Renato Zanetti[1] and Ryan P Russell[1]

[1]Department of Aerospace Engineering and Engineering Mechanics, The University of Texas at Austin, Austin, Texas 78712, USA.

*Corresponding author(s). E-mail(s): jack.a.joshi@my.utexas.edu;
Contributing authors: renato@utexas.edu;
ryan.russell@austin.utexas.edu;

Abstract

Navigation using star occultation measurements can make use of the spacecraft's existing star tracker hardware, commonly included for attitude determination, to derive position information. Although the measurements are inherently time-based, they can be mapped to position- or angle-based models to obtain an explicit algebraic measurement function. This paper proposes an elevation angle approach for processing star occultations and compares it with two existing measurement formulations. Importantly, the elevation angle model ensures that the camera detection error remains independent of the state and consistently Gaussian within the filter. The scenario considered is a spacecraft operating in an Earth-Moon $\boldsymbol{L_2}$ southern near rectilinear halo orbit (NRHO) with an onboard extended Kalman filter. Since the frequency of occultation measurements is dependent on the dynamics, the NRHO provides an interesting example with substantial variation in spacecraft velocity. The feasibility of all three measurement approaches is assessed in terms of filter consistency, measurement nonlinearity, and overall robustness.

Keywords: Star occultation, elevation angle, star tracker, cislunar space

1 Introduction

As NASA's Artemis program seeks to send humans back to the Moon for the first time in fifty years, optical navigation is emerging as a viable navigation source. This gives

rise to new possibilities where combining optical navigation techniques with existing star tracker technology can enable several measurement options. For example, the use of a star tracker has been explored to obtain position information, through observing the direction of planets relative to the spacecraft, by Mortari and collaborators [1, 2]. Additionally, full pose estimation can be performed using a separate onboard camera providing landmark-based imagery, which becomes greatly simplified when a star tracker is available for attitude estimation [3]. A star tracker itself can also be repurposed to detect both star occultations, which provide position information, and other non-occulted stars in the field of view (FOV), to obtain attitude information, which is particularly relevant to this work. Detecting these occultations is enabled by modern high performance star trackers, such as the ones onboard Orion, that are able to accurately detect stars even with the Moon in the FOV. While modern technology is better equipped to support occultation measurements, these measurements were originally introduced in the 1960s [4–7] and tested onboard the Earth-orbiting Gemini VII and X missions, with an expected root mean square error (RMSE) in spacecraft position of one nautical mile [8]. Since then, they have been explored as standalone measurement sources in the literature [9–11].

Fundamentally, a star occultation measurement is the time tag recorded when the observer, or onboard camera, detects the occultation of a star by a third object with a known position, such as the Moon. To increase the measurement frequency, the time at which a star either disappears or reappears from behind the lunar limb is recorded. These occultations can only be detected along the dark lunar limb though, as the illuminated side is too bright to precisely determine when a star disappears or reappears. Ideally, the associated time tag would then be used directly as a time-based measurement, since navigation filters perform best when the measurement is processed as little as possible and remains close to the raw hardware output, thereby preserving well-characterized, state-independent error characteristics [12]. However, because time is traditionally treated as the independent variable in filtering, a predicted time of occultation cannot be obtained explicitly, and the resulting time-based measurement function is implicit. To find an explicit representation, Psiaki and Hinks [10] map the occultation measurement into a distance-based metric. While their approach has proven effective, by both Psiaki and Hinks as well as Crouse [11], the elevation-angle formulation proposed in this paper provides a comparable alternative while preserving state-independent camera detection error characteristics. Furthermore, the filter framework outlined here directly incorporates time-tag uncertainty into the predicted measurement time, which was not previously considered.

In this paper, the newly-proposed elevation angle model is considered and a survey of existing occultation measurement approaches, namely minimum altitude [10] and time [9] models, is also performed. Figure 1 visualizes these three approaches—labeled models 1, 2, and 3—for the case in which the Moon occults the jth star, shown relative to the true location of the spacecraft in green. The true and predicted measurements for the elevation angle (ε), minimum altitude (h), and time (t) models are indicated, with overbars $\bar{(\cdot)}$ denoting predicted values and $(\cdot)_m$ denoting values evaluated at the measured occultation time t_m. Additionally, the true ($\boldsymbol{x}$) and predicted ($\bar{\boldsymbol{x}}$) states are shown.

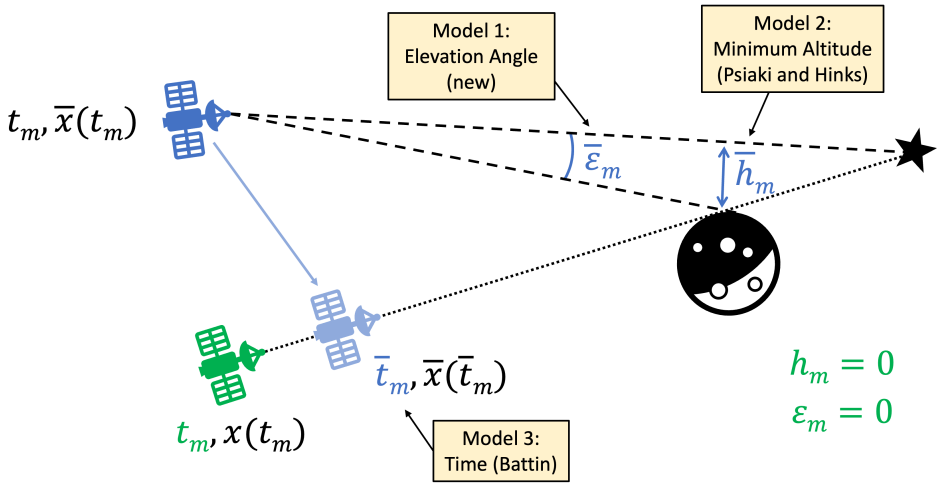


Fig. 1 The three occultation measurement models are visualized with the true and predicted measurements shown in green and blue, respectively.

In order to compare and contrast the three approaches, a 9:2 near rectilinear halo orbit (NRHO) from the L_2 southern halo orbit family is used, arising from the circular restricted three-body problem (CR3BP) dynamics. Although the NRHO is a mildly unstable orbit, the orbit can be maintained with consistent but small station-keeping maneuvers. NRHOs in the Earth-Moon system were of particular interest for the Artemis program and, specifically, Gateway because of their ability to provide cheap transfers in terms of Δv consumption [13, 14]. While Gateway has since been paused [15], the NRHO still provides a valuable nonlinear scenario due to its low perilune and high apolune altitudes. Since the NRHO is a highly elliptical orbit, it also produces large variability in the velocity of the spacecraft. This variability makes star occultations an interesting example, as the frequency of occultation measurements is directly tied to the dynamics of the spacecraft. In particular, it is expected that there will be minimal measurements near apolune and an increasing number of measurements as the spacecraft approaches perilune. However, when the spacecraft is close to perilune, the large apparent size of the Moon may obstruct much of the camera's field of view (FOV), limiting the number of available occultation measurements.

All of this is explored in more depth in the remainder of the paper. In Section 2, the three distinct star occultation measurement models are derived, and their shared error sources are then discussed in Section 3. The system dynamics are provided in Section 4 along with the filter, sensor, and environment details. The corresponding results are then presented in Section 5, showcasing the effectiveness of each measurement model, before the approaches are distinguished from each other in Section 6. Finally, future work is discussed in Section 7, concluding remarks are made in Section 8, and relevant derivations are included in the Appendix.

2 Star Occultation Measurement Models

Star occultations provide a time tag that can be treated as a measurement. The difficulty, though, arises when the time-based measurement is incorporated into a filter, as it is difficult to obtain a closed-form analytic expression of the time measurement as a function of the spacecraft state (position and velocity). Consequently, the corresponding measurement function, and hence the predicted time measurement, must be obtained by solving an implicit equation. To limit the nonlinearity of the measurement function, two approaches are considered that transform the occultation measurement into either position or angle space. The former is an existing methodology, while the latter is a new contribution of this work. The three models are presented in reverse chronological order though, since the time-based implementation relies on the elevation angle derivation.

2.1 Elevation Angle

The proposed approach is to define the occultation measurement in terms of the elevation angle of the star above the Moon's limb. This formulation specifically allows the camera detection error to remain additive within the filter. Elevation angle measurements were suggested as an optical navigation source for Orion for loss-of-signal scenarios [16] and are adapted for occultation measurements here. An occultation occurs when the measured elevation angle is zero,

$$z_m = 0, \tag{1}$$

where the subscript $(\cdot)_m$ corresponds to the measured occultation time, t_m. The predicted measurement, $\bar{z}$, is then defined as

$$\bar{z}_m = \bar{\varepsilon}_m = \varepsilon(t_m, \bar{\boldsymbol{x}}), \tag{2}$$

with $\bar{\varepsilon}$ being the predicted elevation angle and $\bar{\boldsymbol{x}}$ being the predicted state. Here, the elevation angle, ε, is defined as

$$\varepsilon = \gamma - \rho \quad \text{with} \quad \gamma = \arccos(-\hat{\boldsymbol{r}} \cdot \hat{\boldsymbol{r}}_*^j) \quad \text{and} \quad \rho = \arcsin\left(\frac{R_{\leftmoon}}{r}\right) \tag{3}$$

where $\boldsymbol{r}$ is the Moon-relative position of the spacecraft, $\boldsymbol{r}_*^j$ is the position vector of the star with respect to the spacecraft, $R_{\leftmoon}$ is the radius of the Moon, and $\hat{(\cdot)}$ denotes a unit vector. In Eqs. (2) and (3), γ is the angle between the line-of-sight vectors from the spacecraft to the Moon and from the spacecraft to the occulting star, and ρ is the apparent angular radius of the Moon, as seen in Figure 2. By representing the elevation angle as the difference between γ and ρ, the elevation angle remains continuously differentiable at $\varepsilon = 0$.

The corresponding measurement partials are non-zero with respect to position,

$$\boldsymbol{H}_r = \frac{1}{r\cos\rho}\boldsymbol{i}_p, \tag{4}$$

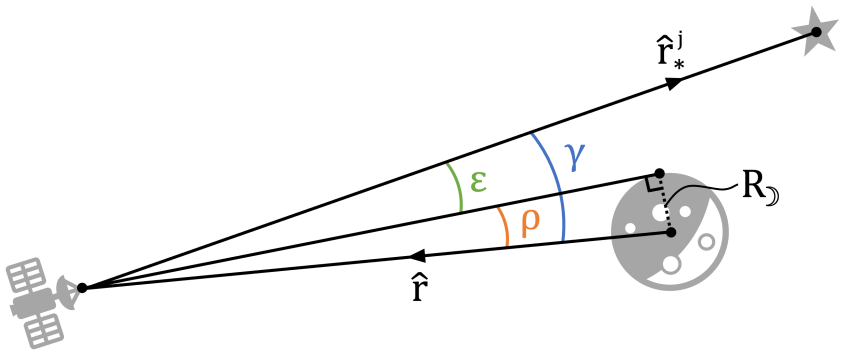


Fig. 2 Elevation angle geometry.

and zero with respect to velocity. In Eq. (4), the unit vector $\boldsymbol{i}_p$ is normal to the line of sight vector from the spacecraft to the Moon's limb while remaining in the measurement plane [9]. Mathematically, $\boldsymbol{i}_p$ is defined as

$$\boldsymbol{i}_p = \cos\rho\ \boldsymbol{i}_n + \sin\rho\ \hat{\boldsymbol{r}} \tag{5}$$

where

$$\boldsymbol{i}_n = \frac{1}{\sin\gamma}(\cos\gamma\ \hat{\boldsymbol{r}} + \hat{\boldsymbol{r}}^j_*) \tag{6}$$

is normal to the Moon-relative position vector, $\boldsymbol{r}$, and also in the measurement plane. Additionally, the measurement partials with respect to the lunar radius bias, H_b, are

$$H_b = -\frac{1}{\sqrt{r^2 - R_☽^2}} \tag{7}$$

Lastly, the variance R (or scalar covariance) of the total measurement error, is given by the sum of the camera detection error, R_{cam}, and the state-dependent time-tag uncertainty, R_{time}, as seen below:

$$R = R_{\text{cam}} + \dot{\bar{\varepsilon}}^2_m R_{\text{time}}. \tag{8}$$

Both of these error sources are discussed in more depth in Section 3.

2.2 Minimum Altitude

Another approach to avoid time as the measurement is to use the minimum distance between the line-of-sight vectors from the spacecraft to the star and from the spacecraft to the limb of the occulting body, as formulated by Psiaki and Hinks [10]. Similar to the elevation angle approach, when the onboard star tracker detects an occultation, the measured minimum distance (or altitude) is zero:

$$z_m = 0. \tag{9}$$

Psiaki and Hinks then define the predicted measurement to be

$$\bar{z}_m = \bar{h}_m, \quad \bar{h}_m = ||\boldsymbol{r}^j_{\min}(\bar{\boldsymbol{x}}_m)|| - R_{\mathbb{D}} \tag{10}$$

which is a function of the predicted state, $\bar{\boldsymbol{x}}$, and the radius of the moon, $R_{\mathbb{D}}$. Additionally, the minimum distance vector, $\boldsymbol{r}^j_{\min}$, for the jth star is geometrically defined as

$$\boldsymbol{r}^j_{\min}(\bar{\boldsymbol{x}}_m) = \bar{\boldsymbol{r}}_m + \alpha_{\min}(\bar{\boldsymbol{x}}_m)\hat{\boldsymbol{r}}^j_*, \qquad \alpha_{\min}(\bar{\boldsymbol{x}}_m) = -(\hat{\boldsymbol{r}}^j_*)^T\bar{\boldsymbol{r}}_m \tag{11}$$

under the assumption that the occultation occurs within a 180° field of view of the spacecraft and the camera is oriented towards the Moon.

Unlike the elevation angle approach though, the camera detection error must be mapped into a state-dependent measurement error within the filter,

$$R = \left(\frac{\boldsymbol{H}f(\bar{\boldsymbol{x}})}{\dot{\bar{\varepsilon}}}\right)^2 R_{\text{cam}} + (\boldsymbol{H}f(\bar{\boldsymbol{x}}))^2 R_{\text{time}}, \tag{12}$$

where $\boldsymbol{H}$ is the corresponding measurement partials with respect to the state and $f(\bar{\boldsymbol{x}})$ is the state dynamics. The measurement partials with respect to velocity, $\boldsymbol{H}_v$, are zero, but with respect to position and the lunar radius bias they are

$$\boldsymbol{H}_r = \left(\hat{\boldsymbol{r}}^j_{\min}\right)^T \left(\boldsymbol{I} - \hat{\boldsymbol{r}}_*\hat{\boldsymbol{r}}^T_*\right) \tag{13}$$

and

$$H_b = -1, \tag{14}$$

respectively. It is also worth mentioning that the vectors $\boldsymbol{r}^j_{\min}$ and $\boldsymbol{H}_r$ in Eqs. (11)-(13) are defined in the Moon-centered inertial frame.

2.3 Time

Lastly, a time-based measurement model will be considered as it reflects the true form of an occultation measurement, at least from a theoretical standpoint. The time-based measurement model was originally proposed for the Apollo program and derived by Battin [9], with an additional approximation taken here to allow for filter implementation. The actual time measurement is the time stamp provided by the sensor when the occultation is detected,

$$z_m = t_m. \tag{15}$$

An implicit equation for the predicted time measurement $\bar{t}_m$ is then given by

$$\varepsilon(t_m, \bar{\boldsymbol{x}}) + \int_{t_m}^{\bar{t}_m} \dot{\varepsilon}\, dt = \varepsilon(\bar{t}_m, \bar{\boldsymbol{x}}) = 0 \tag{16}$$

where the time derivative of ε in Eq. (3) is

$$\dot{\varepsilon} = \frac{\boldsymbol{v}_r \cdot \dot{\boldsymbol{i}}_p}{r\cos\rho} \tag{17}$$

and specific care is taken to ensure that the sign of $\dot{\varepsilon}$ is physically intuitive. In Eq. (17), $\boldsymbol{v}_r$ is the spacecraft's relative velocity and r is the relative position magnitude. Unless otherwise specified, all quantities labeled as "relative" are with respect to the Moon.

Solving for $\bar{t}_m$ in Eq. (16) to obtain an explicit formula for the time measurement is generally not possible in closed form, and some numerical solution needs to be employed. One possibility is to expand $\varepsilon(t, \bar{\boldsymbol{x}})$ in a Taylor series centered at the measured occultation time, and then root-solve the equation. If the series is truncated to first order, the solution is simply

$$\bar{t}_m \approx t_m - \frac{\varepsilon(t_m, \bar{\boldsymbol{x}})}{\dot{\varepsilon}(t_m, \bar{\boldsymbol{x}})} \tag{18}$$

and the predicted occultation time measurement is

$$\bar{z}_m = \bar{t}_m \approx t_m - \frac{\bar{\varepsilon}}{\dot{\bar{\varepsilon}}} \tag{19}$$

in terms of the predicted elevation angle, $\bar{\varepsilon} = \bar{\varepsilon}(t_m, \bar{\boldsymbol{x}})$, and its rate of change, $\dot{\bar{\varepsilon}}$. This predicted measurement formulation makes sense intuitively because if the predicted elevation angle is positive ($\bar{\varepsilon} > 0$) and the star is disappearing behind the Moon ($\dot{\bar{\varepsilon}} < 0$), then the occultation is expected to occur in the future ($\bar{t}_m > t_m$). The intuition also holds for the other possible values of $\bar{\varepsilon}$ and $\dot{\bar{\varepsilon}}$.

For a single eight-hour perilune pass, as discussed in Section 4, the maximum relative error between the first-order Taylor series approximation and the root-solved predicted occultation time is 6.055×10^{-4}. This is equivalent to a minimum accuracy of 99.94%, indicating that the first-order approximation is sufficient. The corresponding fully expanded measurement partials are included in Appendix A, but the general form is

$$\boldsymbol{H}_r^* = -\frac{1}{\boldsymbol{v}_r \cdot \boldsymbol{i}_p} \boldsymbol{i}_p^T + \left(\frac{\varepsilon}{\dot{\varepsilon}^2}\right) \boldsymbol{v}_r^T \frac{\partial^2 \varepsilon}{\partial \boldsymbol{r} \partial \boldsymbol{r}^T}, \tag{20}$$

$$\boldsymbol{H}_v^* = \frac{\varepsilon r \cos\rho}{(\boldsymbol{v}_r^T \boldsymbol{i}_p)^2} \boldsymbol{i}_p^T, \tag{21}$$

and

$$H_b^* \approx \frac{1}{\dot{\varepsilon}\sqrt{r^2 - R_{\mathbb{D}}^2}} - \frac{\varepsilon R_{\mathbb{D}}}{\boldsymbol{v}_r^T \boldsymbol{i}_p \sqrt{r^2 - R_{\mathbb{D}}^2}}. \tag{22}$$

It is important to note that the partials in Eqs. (20)-(22) above reflect the predicted measurement function in Eq. (19). Additionally, while the time-tag uncertainty now becomes additive within the filter, the camera detection error remains state dependent when computing the measurement error covariance,

$$R = \frac{1}{\dot{\bar{\varepsilon}}^2} R_{\text{cam}} + R_{\text{time}}. \tag{23}$$

While this time-based approach is expected to be effective for the majority of scenarios, there are two specific edge cases where it may be disadvantageous relative to the other models. First, if the spacecraft is moving such that $\dot{\varepsilon} \approx 0$, a divide-by-zero error could arise when evaluating the predicted time measurement. More generally

though, there may be a situation where a physical occultation occurs but the filter predicts that the event will never happen given the current state estimate. The time-based approach would produce an undefined predicted measurement in this case, preventing the filter from gaining new information. However, the elevation angle and minimum altitude models are robust to this scenario, as they would still produce a finite predicted measurement, enabling the measurement update.

3 Modeling and Measurement Errors

Each of the measurement models discussed above is subject to the same measurement errors and modeling choices. However, some models are better at limiting approximations and preserving the underlying assumptions associated with specific error sources. The three main error sources, time-tag uncertainty, camera detection error, and lunar radius error, are discussed in this section, along with parallax and stellar aberration.

3.1 Camera Detection Error

The main source of sensor-based error included in this work is the camera detection error, $w_{\text{cam}} \sim \mathcal{N}(0, R_{\text{cam}})$. Fundamentally, this measurement error is a pixel-based error, w_{pixel}, that corresponds to the uncertainty induced when locating the star in the focal plane. However, this can be converted into an angular error using camera parameters via

$$w_{\text{cam}} = \text{IFOV} * w_{\text{pixel}}, \quad \text{IFOV} = \frac{a_{\text{pixel}}}{f}, \tag{24}$$

where a_{pixel} is the pixel pitch, f is the focal length of the camera, and IFOV is the instantaneous field of view. For the elevation angle approach, the camera detection error remains additive whereas, for the other two approaches, this error becomes state-dependent in the onboard filter. Hence, the elevation angle model allows the camera detection error to better reflect the hardware.

Within the simulation, the camera detection error perturbs the true occultation time, t_m^*, via

$$t_m^* = t_{\text{nom}}^j + \frac{1}{\dot{\varepsilon}} w_{\text{cam}} \tag{25}$$

where t_{nom}^j is the nominal time of occultation for the jth star. This formulation is derived from a first-order Taylor series expansion and is considered sufficient given the small angular errors. This assumption is supported by a maximum relative error of 9.831×10^{-5} compared to the full root-solving solution across a single eight-hour perilune pass. The maximum relative error equates to a minimum accuracy of 99.99% for the first-order approximation in Eq. (25).

3.2 Time-Tag Uncertainty

While the measurement would ideally be processed at the true occultation time, the measured time received by the filter is naturally corrupted by some time-tag uncertainty. This uncertainty primarily consists of two random components: jitter, which

is treated as being Gaussian-distributed, and quantization error, which follows a uniform distribution. For ease of implementation within the filtering framework, both of these error sources are encompassed in the δt_k term below

$$\delta t_k \sim \mathcal{N}(0, R_{\text{time}}) \tag{26}$$

which is modeled as zero-mean Gaussian white noise. It is important to note that this Gaussian assumption is a practical filtering consideration and not a limitation of the proposed measurement model. The noise then affects the measured occultation time, t_m, via

$$t_m = t_m^* + \delta t_k \tag{27}$$

which dictates when the measurement is processed within the filter. In reality though, the true occultation time is unknown and the onboard filter would only receive the noisy measurement time stamp, t_m.

3.3 Terrain Uncertainty

The timing of star occultations is also affected by morphology and uncertainty associated with the lunar terrain. Here, the true lunar terrain is modeled by perturbing a spherical surface using a spatially correlated first-order Gauss-Markov (FOGM) process. This approach is taken over a more realistic shape model for the truth in order to limit the computational complexity. A simpler model is included onboard, in which a time-correlated FOGM process is used with a tuned time constant. The general modeling of the biases as FOGM processes is motivated by the approach being deemed a "best practice" [17].

The spatially correlated bias, b, evolves as the camera image virtually traverses the lunar surface, and perturbs the average lunar radius, $R_{\text{☽,avg}}$, to obtain the "true" lunar radius, $R_{\text{☽}}$,

$$R_{\text{☽},k} = R_{\text{☽,avg}} + b_k, \tag{28}$$

at time t_k. This true bias is modeled as a spatially-correlated FOGM process via

$$\dot{b} = -||\boldsymbol{V}^M|| \frac{1}{\delta} b, \quad \boldsymbol{V}^M = \dot{\boldsymbol{R}}_{\text{☽}}^M, \tag{29}$$

where $\dot{(\cdot)}$ indicates a time derivative, the superscript M denotes the Moon-centered Moon-fixed frame, δ is the correlation distance, and $\boldsymbol{R}_{\text{☽}}$ is the lunar radius vector at the point of the surface where the camera is centered. The homogeneous solution of Eq. (29) is integrated using a fourth- and fifth-order Runge-Kutta scheme and the process noise, ν_b, is then added discretely,

$$b_k = F_{k-1}(b_{k-1}) + \nu_{b,k-1}, \tag{30}$$

which allows the bias to wander and represents the non-spherical and uncertain nature of lunar terrain. The process noise discretization is adapted from Carpenter and D'Souza [17] and is given by

$$\nu_{b,k-1} \sim \mathcal{N}(0, Q_{b,k-1}), \quad Q_{b,k-1} = P_{b,0}\left(1 - e^{-2||\boldsymbol{V}^M||\Delta t/\delta}\right), \tag{31}$$

where Δt is the simulation time step. Without measurements, this formulation would ensure that the bias uncertainty maintains a steady-state value equal to the initial variance, $P_{b,0}$.

The onboard filter model differs from the above "true" model and consists of a simpler time-correlated bias. The modeled filter bias, $\bar{b}$, is subject to the following dynamics

$$\dot{\bar{b}} = -\frac{1}{\tau}\bar{b} \tag{32}$$

and is used to compute the predicted lunar radius

$$\bar{R}_{\text{☽},k} = R_{\text{☽,avg}} + \bar{b}_k. \tag{33}$$

In Eq. (32), τ is the correlation time or time constant, and process noise is excluded to ensure the statistical consistency of the Monte Carlo analysis. In the absence of process noise, τ is set to be sufficiently large such that the filter biases are effectively constant to prevent them from decaying to zero. This approach allows the filter biases to remain decoupled from each other while ensuring that the N filter trajectories are deterministic, complying with the Monte Carlo approach discussed in Section 4.2.1.

Similar to the truth model, the process noise associated with the filter bias is defined such that the initial and steady-state covariances are equal,

$$Q_{\bar{b},k-1} = P_{b,0}\left(1 - e^{-2\Delta t/\tau}\right), \tag{34}$$

where $e^{-2\Delta t/\tau}$ goes to zero as τ approaches infinity [17]. This definition allows the uncertainty to remain fixed and is consistent with the bias being considered in the filter but not estimated. Given the fixed uncertainty, along with the discrepancy between the truth and filter models, the filter performance may be slightly conservative. While a higher-fidelity lunar terrain model could be included in both models, a conservative approach is taken here to focus on the measurement models themselves.

3.4 Other Modeling Choices

Two additional effects are also relevant to consider: parallax and stellar aberration. Since the stars are assumed to be sufficiently far away, parallax is deemed negligible. This assumption is further supported by data suggesting a maximum stellar parallax-induced error of 0.78 arcseconds when observing an occultation [18], which is much less significant than other error sources. In particular, the expected maximum error associated with stellar aberration is two orders of magnitude larger, approximately 20.4 arcseconds [18], based on the heliocentric velocity of Earth. Therefore, the effects of stellar aberration must be included and may actually be slightly larger due to the added velocity of the observer (or spacecraft) relative to Earth in this cislunar example.

Fundamentally, stellar aberration affects the perceived location of potentially occulting stars and, specifically, the corresponding unit vector

$$\hat{\boldsymbol{r}}_*^+ = \text{Unit}\left(\hat{\boldsymbol{r}}_* + \frac{\boldsymbol{v}_{\text{rel}}}{c}\right) \tag{35}$$

where $\boldsymbol{v}_{\text{rel}}$ is spacecraft's velocity relative to the center of the inertial frame, c is the speed of light, $\hat{\boldsymbol{r}}_*$ is the unit position vector of the star in the inertial frame, and $\hat{\boldsymbol{r}}_*^+$ is the updated unit vector. This adjustment affects both the timing of the true occultations and the measurement prediction. It is also important to note that the uncertainty in $\hat{\boldsymbol{r}}_*^+$ due to the uncertainty in v_{rel} is deemed negligible under the assumption that $v_{\text{rel}} \lll c$.

3.5 Measurement Model Summary

Table 1 A comparison of star occultation measurement models based on the measurement function and error sources.

Model	Measurement Function	Detection Error	Time-Tag Uncertainty	Terrain Modeling Error
Time	Implicit, highly nonlinear	State-dependent white noise	Additive white noise	Gauss-Markov radius bias
Minimum Altitude	Explicit analytical formulation	State-dependent white noise	State-dependent white noise	Gauss-Markov radius bias
Elevation Angle	Explicit analytical formulation	Additive white noise	State-dependent white noise	Gauss-Markov radius bias

The primary error sources and the measurement function for each model are summarized in Table 1. As the table shows, both the minimum altitude and elevation angle approaches have an explicit measurement function that avoids the need to root-solve or truncate higher-order terms. However, only the elevation angle approach allows the camera detection error to remain additive within the filter. While the other two primary error sources are consistent between the angle and altitude measurement models, they are modeled with higher fidelity than in previous work. For example, Psiaki and Hinks [10] modeled the terrain error as white Gaussian noise, whereas the terrain's spatial correlation is included, via a Gauss-Markov radius bias, in this paper. The bias, which is treated by the onboard filter as a consider parameter, allows the terrain error to be correlated over time and ensures that the filter is conservative. Additionally, the time-tag uncertainty directly perturbs the measured time, t_m, providing a more natural formulation than the traditional measurement noise approach. For completeness, all three models are compared, and the nonlinearity of each measurement model is discussed in more depth in Section 6.

4 Cislunar Orbit Determination Scenario

In order to simulate how each measurement model performs with the various error sources included, a cislunar orbit determination scenario is considered. This scenario is motivated by the increasing occupation of cislunar space and, specifically, NASA's plan for a long-term presence on and around the Moon. The goal is to provide a

realistic scenario that evaluates the feasibility of star occultation measurements and explores effective ways to represent them in the filter. The chosen cislunar orbit, the onboard filter, the sensor specifications, the simulation environment, and the initial simulation parameters are all discussed in this section.

4.1 CR3BP Dynamics

This orbit determination scenario leverages the circular restricted three-body problem (CR3BP) dynamics. In the Earth-Moon synodic frame, the corresponding equations of motion are

$$\ddot{r}_x - 2\dot{r}_y = \frac{\partial U}{\partial r_x}, \quad \ddot{r}_y + 2\dot{r}_x = \frac{\partial U}{\partial r_y}, \quad \ddot{r}_z = \frac{\partial U}{\partial r_z} \tag{36}$$

where r_x, r_y, and r_z parameterize the spacecraft's position in the rotating Earth-Moon frame. Equation (36) is also defined in terms of the following potential function

$$U = \frac{1}{2}\left(r_x^2 + r_y^2\right) + \frac{1-\mu}{\rho_{\oplus}} + \frac{\mu}{\rho_{\moon}} \tag{37}$$

with μ being the following non-dimensional gravitational parameter

$$\mu = \frac{\mu_{\moon}}{\mu_{\oplus} + \mu_{\moon}}, \tag{38}$$

and $\rho_{\oplus}$ and $\rho_{\moon}$ are the non-dimensional distances of the spacecraft relative to the Earth and Moon, respectively,

$$\rho_{\oplus} = \sqrt{\left(r_x^2 + \mu\right)^2 + r_y^2 + r_z^2}, \qquad \rho_{\moon} = \sqrt{\left(r_x^2 - 1 + \mu\right)^2 + r_y^2 + r_z^2}. \tag{39}$$

In Eq. (38), $\mu_{\oplus}$ is Earth's gravitational parameter and $\mu_{\moon}$ is the Moon's gravitational parameter. The non-dimensional distances are normalized using the characteristic length, l^*, and time, t^*, for the Earth-Moon system. These values along with other Earth-Moon system parameters are included in Table B4. Using those parameters, the CR3BP dynamics are integrated using an adaptive fourth- and fifth-order Runge-Kutta scheme.

4.1.1 Near-Rectilinear Halo Orbit

Within the CR3BP realm, an Earth-Moon 9:2 NRHO [19] from the southern halo orbit family about L_2 is considered, as seen in Figure 3. This orbit was particularly relevant, as it was expected to be the home of NASA's Gateway mission and visited by Orion, among other vehicles [20]. Still, the NRHO naturally provides a wide range of occultation measurement frequencies, making it an interesting example. Near apolune, when the spacecraft's angular velocity relative to the Moon is minimal, star occultations are infrequent. As a result, an additional measurement source, such as the apparent lunar radius [21, 22], may be necessary to complement star occultations and provide position information in occultation-sparse regions. However, near perilune, aside from when the Moon obstructs the camera's FOV, star occultations are much more frequent because of the fast-moving Moon-relative dynamics. Because of the high measurement

frequency, occultations can be considered as a standalone measurement source in that region.

While CR3BP dynamics are used here, the fundamental orbit geometry is maintained as the NRHO is transitioned into higher fidelity models, such as the Hill restricted four-body problem (HR4BP) or full ephemeris models. In the HR4BP, for example, the periodic orbit transitions into families of periodic orbits, based on the continuation initialization point and the relative location of the Sun [23]. This implies that the NRHO that persists in higher fidelity models is no longer unique, but the orbit still resembles the general structure seen in the CR3BP. As a result, the performance of the occultation measurements here is expected to be representative of the behavior in a more complex dynamical system.

4.2 Environment, Sensor, and Filter Setup

To focus solely on the occultation measurements themselves, an eight-hour portion of the NRHO trajectory near perilune is considered in Sections 5 and 6, and shown in the top right of Figure 3.

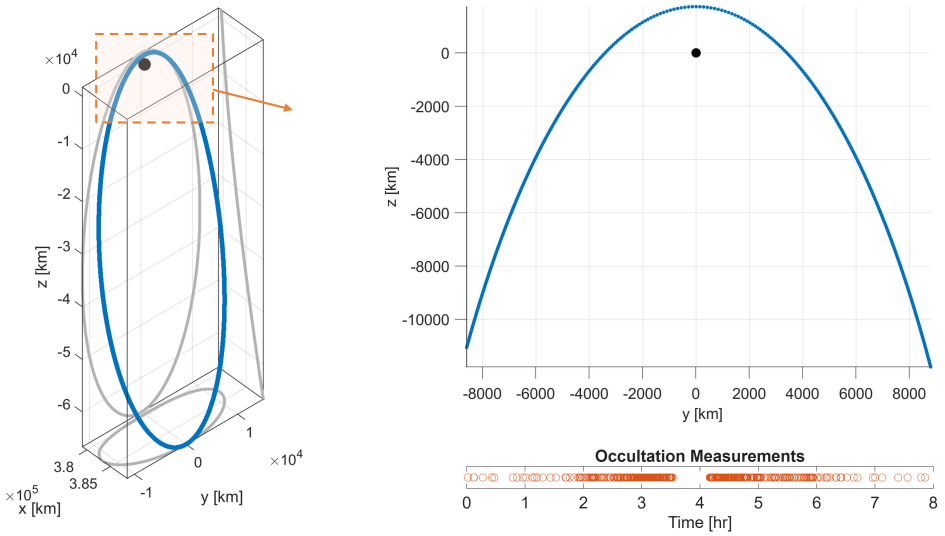


Fig. 3 The full 9:2 NRHO in the Earth-Moon rotating frame (left), an eight-hour portion of the trajectory near perilune (top right), and the corresponding measurement frequency (bottom right).

The bottom right of Figure 3 shows the frequency of occultations, with the darker blue regions indicating a denser cluster of measurements. For the most part, these denser regions are closer to perilune. However, near the four-hour mark, there is a roughly half-an-hour period of no occultation measurements. This blackout happens because the Moon obstructs the camera's FOV, leading to limited visibility of any possibly

occulting stars. If the camera had a larger FOV or there were additional cameras onboard, the blackout could be mitigated though.

Within the simulation environment, the stars are generated using the Hipparcos catalog [24] and are fixed in the inertial frame. All stars of magnitude less than or equal to 6.0 are included, consistent with the Jena-Optronik star tracker used onboard Orion [25]. This threshold amounts to just over 5000 stars, providing a realistic stellar landscape for the camera to survey.

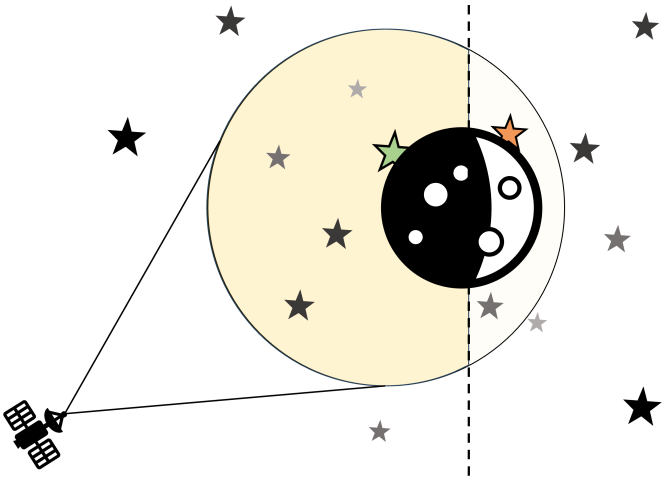


Fig. 4 A depiction of a camera observing an occultation (of the green star) through the circular FOV in the 2D camera plane.

The star tracker, or camera, is assumed to have the ability to detect stars both disappearing behind the Moon as well as reappearing. The associated circular FOV is set to 20 degrees according to the Jena-Optronik star tracker specifications. Occultations can only be observed along the dark limb of the Moon and when the Moon is less than 80% full (or bright). The former is visualized on the right side of Figure 4 where the FOV is highlighted by the yellow circle, and both the green and orange stars are in the process of being occulted by the Moon. However, since only the green star is being occulted along the dark limb, only one occultation can be observed in this example. While having simultaneous occultations may be a relatively rare phenomenon, this example provides an idea of when star occultations can and cannot be observed.

In order to isolate the different measurement models, star occultations are the only form of measurement received by the spacecraft in this scenario. As a result, the frequency of the occultations, and the information they provide about the spacecraft's state, are important to understand.

4.2.1 Filtering Approach

To assess the performance of the different measurement models, an extended Kalman filter (EKF) is used, where the nonlinear dynamics and measurement functions are

linearized about the state estimate via a first-order Taylor series approximation. The framework is similar to the traditional Kalman filter that was originally designed to be optimal in a minimum mean-square-error (MMSE) sense for linear systems with additive Gaussian noise [26, 27]. However, it was later extended for nonlinear systems, in the form of the EKF [28], albeit no longer guaranteeing optimality.

Because it relies on a linearization about the current state estimate, the EKF assumes that the estimate is sufficiently close to the truth. As a result, the highly dynamic perilune region poses a potential challenge that could lead to filter divergence. Nevertheless, as Section 5 will show, relatively frequent measurements allow the estimated state and covariance to accurately capture the true behavior. For this reason, the EKF provides a simple but effective filtering framework that can isolate the behavior of the different measurement models.

The onboard filter state is comprised of the spacecraft's estimated position and velocity, $\hat{\boldsymbol{r}}_k$ and $\hat{\boldsymbol{v}}_k$, along with the predicted lunar radius bias, $\bar{b}_k$,

$$\hat{\boldsymbol{x}}_k = \left[\hat{\boldsymbol{r}}_k^T, \hat{\boldsymbol{v}}_k^T, \bar{b}_k\right]^T, \tag{40}$$

at the current time, t_k. The state is then propagated and updated using the procedure outlined in Eqs. (41)-(47). First, the previous state estimate, $\hat{\boldsymbol{x}}_{k-1}$, is propagated through the nonlinear dynamics via the transition function, $\boldsymbol{F}_{k-1}$,

$$\bar{\boldsymbol{x}}_k = \boldsymbol{F}_{k-1}\left(\hat{\boldsymbol{x}}_{k-1}\right) \tag{41}$$

to produce the predicted state, $\bar{\boldsymbol{x}}_k$. The dynamics are then linearized about the state estimate, $\hat{\boldsymbol{x}}_{k-1}$, to derive the state transition matrix, $\boldsymbol{\Phi}_{k-1}$, which is used to produce the *a priori* covariance, $\bar{\boldsymbol{P}}_k$,

$$\bar{\boldsymbol{P}}_k = \boldsymbol{\Phi}_{k-1}\boldsymbol{P}_{k-1}\left(\boldsymbol{\Phi}_{k-1}\right)^T + \boldsymbol{Q}_{k-1}, \tag{42}$$

with $\boldsymbol{Q}_{k-1}$ being the process noise covariance matrix.

Regardless of whether any star occultations occur between t_{k-1} and t_k, $\hat{\boldsymbol{x}}_k = \bar{\boldsymbol{x}}_k$ and $\boldsymbol{P}_k = \bar{\boldsymbol{P}}$ are defined post-propagation to ensure consistency in the subsequent notation. If one or more occultation measurements are received, they must be processed accordingly. In general, to process a measurement that occurs in between consecutive filter times, the predicted state and covariance at the current time step, t_k, can be "rewound" to the measured occultation time, t_m [29]. Both the predicted measurement, $\bar{z}_m$, and the measurement partials with respect to the state, $\boldsymbol{H}_k$, depend on quantities evaluated at t_m,

$$\bar{z}_m = h\left(\bar{\boldsymbol{x}}(t_m)\right), \qquad \boldsymbol{H}_k = \left.\frac{\partial h}{\partial \boldsymbol{x}}\right|_{\bar{\boldsymbol{x}}(t_m)} \boldsymbol{\Phi}(t_m, t_k), \tag{43}$$

with h being the measurement function in Eq. (43). This approach provides a more accurate prediction of the true measurement while still mapping it back to the current filter time step via $\boldsymbol{H}_k$.

The mapping effect can be seen more clearly with the algorithm outlined below, resembling the traditional EKF form in the case of a single measurement. However, when multiple occultations occur within a single filter time step, the measurements

are processed sequentially in an order-invariant manner [17]. First, the change in the state estimate is determined,

$$\delta\hat{\boldsymbol{x}}_k = \delta\hat{\boldsymbol{x}}_k + \boldsymbol{K}_k\left(z_m - \bar{z}_m + \boldsymbol{H}_k\delta\hat{\boldsymbol{x}}_k\right), \tag{44}$$

where $\delta\hat{\boldsymbol{x}}_k$ is zero initially and the true measurement is modeled as being noisy. Additionally, the Kalman gain, $\boldsymbol{K}_k$, is defined as

$$\boldsymbol{K}_k = \bar{\boldsymbol{P}}_k\left(\boldsymbol{H}_k\right)^T\left[\boldsymbol{H}_k\bar{\boldsymbol{P}}_k\left(\boldsymbol{H}_k\right)^T + R\right]^{-1}. \tag{45}$$

The covariance is then updated to obtain the *a posteriori* covariance

$$\boldsymbol{P}_k = \left(\boldsymbol{I} - \boldsymbol{K}_k\boldsymbol{H}_k\right)\boldsymbol{P}_k\left(\boldsymbol{I} - \boldsymbol{K}_k\boldsymbol{H}_k\right)^T + \boldsymbol{K}_k R\left(\boldsymbol{K}_k\right)^T. \tag{46}$$

From there, Eqs. (44)-(46) are repeated until each measurement between t_{k-1} and t_k is processed. The *a posteriori* covariance is updated along the way, whereas the state estimate is computed after all measurements have been processed,

$$\hat{\boldsymbol{x}}_k = \hat{\boldsymbol{x}}_k + \delta\hat{\boldsymbol{x}}_k. \tag{47}$$

It is also important to note again that the lunar radius bias is *considered* [30] and not estimated, meaning that Eqs. (44)-(47) only update the position and velocity components of the state estimate and its covariance. Since the precise timing of the occultations is critical, this modified EKF approach allows the filter to account for measurement latency and time-tag uncertainty. Additionally, multiple measurements can be processed sequentially using a batch-like process so that all available information is included.

5 Filter Performance

In order to assess filter performance for each of the measurement models, a Monte Carlo analysis is conducted. In the interest of reducing time complexity, a single truth trajectory is generated with the nominal occultation times recorded. Next, N filter trajectories are initialized, and the corresponding states and covariances are updated using the modified EKF algorithm described in Section 4.2.1. This process is based on the Monte Carlo approach outlined by Maybeck [12] and is repeated for each of the three different star occultation measurement models. The three models are evaluated using consistency and accuracy metrics given the initial conditions provided in this section.

5.1 Initial Conditions and Error Parameters

For the Monte Carlo analysis, the true initial position and velocity of the spacecraft are

$$\boldsymbol{r}_0 = [0.990736, -0.0223382, -0.0287614]^T \tag{48}$$

and

$$\boldsymbol{v}_0 = [-0.0645360, 0.1952886, 0.7177936]^T, \tag{49}$$

and the true initial lunar radius bias is $b_0 = 0$. Together, these form the true initial augmented state,

$$\boldsymbol{x}_0 = \left[\boldsymbol{r}_0^T, \boldsymbol{v}_0^T, b_0\right]^T. \tag{50}$$

These parameters, along with the values in Eq. (53), are non-dimensionalized based on the characteristic length, l^*, and time, t^*, of the Earth-Moon CR3BP system.

To initialize the filter, N states are then randomly generated from the initial Gaussian distribution

$$\hat{\boldsymbol{x}}_0^{(i)} \sim \mathcal{N}(\boldsymbol{x}_0, \boldsymbol{P}_0), \quad i = 1, ..., N, \tag{51}$$

where

$$\boldsymbol{P}_0 = \text{diag}([\sigma_r, \sigma_r, \sigma_r, \sigma_v, \sigma_v, \sigma_v, \sigma_b]^2) \tag{52}$$

and

$$\sigma_r = 2.5 \times 10^{-5}, \;\; \sigma_v = 1 \times 10^{-4}, \;\; \sigma_b = 2.6 \times 10^{-7}. \tag{53}$$

The position and velocity covariances are defined based on values from Boone et al. [31] and adapted for a spacecraft starting near perilune. Additionally, since there is no mismatch between the true and filter dynamics, the only non-zero component of the process noise matrix, $\boldsymbol{Q}$, is the lunar radius bias component, $Q_{\tilde{b}}$, which is defined in Section 3.

The modeling error associated with this bias, σ_b, is provided in its dimensionalized form in Table 2 below, along with the other two primary error sources. The 100-meter lunar radius error is conservative given the topographical maps obtained by the Lunar Reconnaissance Orbiter [32] but reflects a scenario where a detailed digital elevation model is not available onboard.

Table 2 Modeling and measurement error source values.

Error Source	1σ Value	Units
σ_b	0.1	km
σ_{cam}	0.5	pixel
σ_{time}	$\Delta t_{\text{cam}}/\sqrt{12}$	s

Next, the camera detection error is represented by σ_{cam} within the filter. While an error of 0.1 pixel is achievable based on modern centroiding algorithms and star tracker performance [33], a conservative value is again chosen for robustness to additional uncertainty. Lastly, the time-tag uncertainty is characterized by σ_{time} and is defined based on the variance of a uniform random variable. σ_{time} is inversely proportional to the camera's frame rate, modeled as 1 Hz here, so $\Delta t_{\text{cam}} = 1$ s. These error sources, initial conditions, and the remaining simulation parameters are all summarized in Appendix B.

5.2 Results

Given the specified initial conditions and error parameters, a set of $N = 1000$ Monte Carlo runs is generated for each of the three measurement models. Since it takes more than two hours to complete each set using a parallel pool of ten workers, the number of samples balances the computational efficiency and overall accuracy of the Monte Carlo analysis. The listed computational time also assumes that the true trajectory with the true occultation times has been pre-computed. The results are included below, and the feasibility of each approach is assessed using several metrics. These include the estimation errors, the scaled normalized estimation error squared (SNEES), and the time-averaged root mean square error (RMSE).

5.2.1 State Estimation Errors

Figure 5 shows the error in the position estimate over time for the elevation angle, minimum altitude, and time measurement models in the green, blue, and orange boxes, respectively. As the spacecraft receives additional occultation measurements, the covariance bounds shrink, indicating that the knowledge of the truth has improved. Additionally, the true and filter covariances, corresponding to the orange dashed and blue solid lines, respectively, match each other well. This agreement indicates consistency in the filter for all three measurement models.

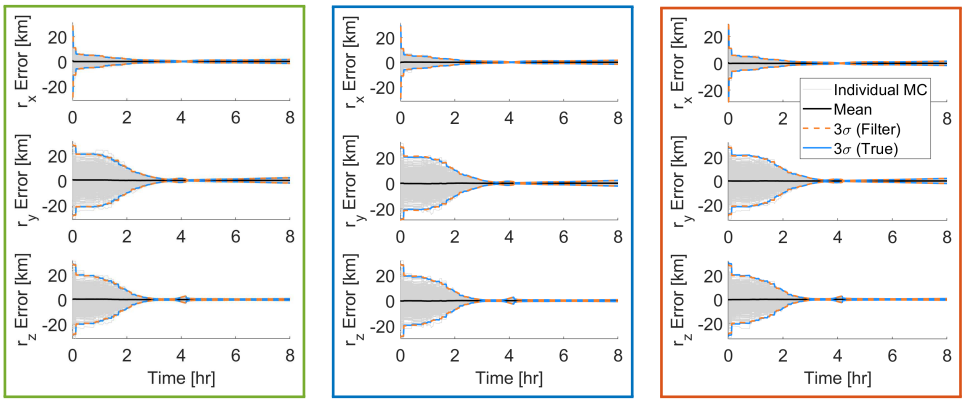


Fig. 5 Position errors for the elevation angle (left), minimum altitude (middle), and time (right) measurement models in the green, blue, and orange boxes, respectively.

To provide more insight into the behavior near perilune, Figure 6 zooms in on the middle portion of the eight-hour trajectory. Just after the four-hour mark, the spacecraft begins to receive occultation measurements again, and the covariance bounds snap back down in the y- and z-directions. This behavior is desired, and the x-, y-, and z-directions here are in the Earth-Moon synodic frame. In general, all three models continue to show similar behavior, albeit the time measurement model results in a slightly more conservative filter.

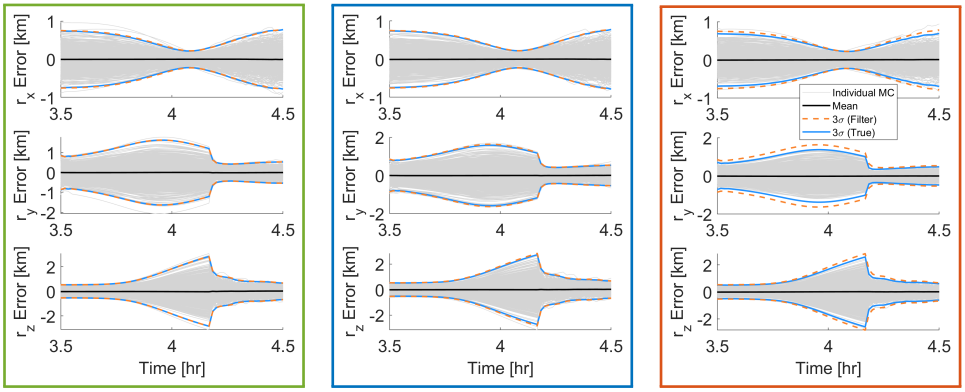


Fig. 6 Position errors near perilune for the elevation angle (left), minimum altitude (middle), and time (right) measurement models in the green, blue, and orange boxes, respectively.

5.2.2 Scaled Normalized Estimation Error Squared

The consistency of the filter is better visualized using the SNEES metric. The SNEES provides a measure of filter consistency with values near unity corresponding to a consistent filter [34]. Furthermore, the filter is conservative if the SNEES is less than one and optimistic for values greater than one. The SNEES at time t_k is shown below

$$\text{SNEES}_k = \frac{1}{nN} \sum_{i=1}^{N} \left[\left(\boldsymbol{\eta}_k^{(i)} \right)^T \left(\boldsymbol{P}_k^{(i)} \right)^{-1} \boldsymbol{\eta}_k^{(i)} \right] \tag{54}$$

where

$$\boldsymbol{\eta}_k^{(i)} = \hat{\boldsymbol{x}}_k^{(i)} - \boldsymbol{x}_k, \qquad i = 1, ..., N \tag{55}$$

with n states and N Monte Carlo runs. In this case, since the lunar radius bias is not being estimated, the SNEES only includes the position and velocity components in the state and covariance terms. The resulting SNEES values for each measurement model are plotted over time in Figure 7.

The magnified plot in Figure 7, whose time axis aligns with the main plot, shows that the time-based approach leads to a slightly more conservative filter. Additionally, when the Moon obstructs the camera's FOV and no measurements are received around the four-hour mark, the SNEES remains constant, as expected without process noise. Overall though, all three measurement models produce consistent filters, especially the elevation angle and minimum altitude models, with SNEES values remaining close to unity.

5.2.3 Root Mean Square Error

In addition to maintaining filter consistency, it is also desirable that the state estimate closely approximates the true state. This accuracy is captured by the RMSE metric, which is defined as

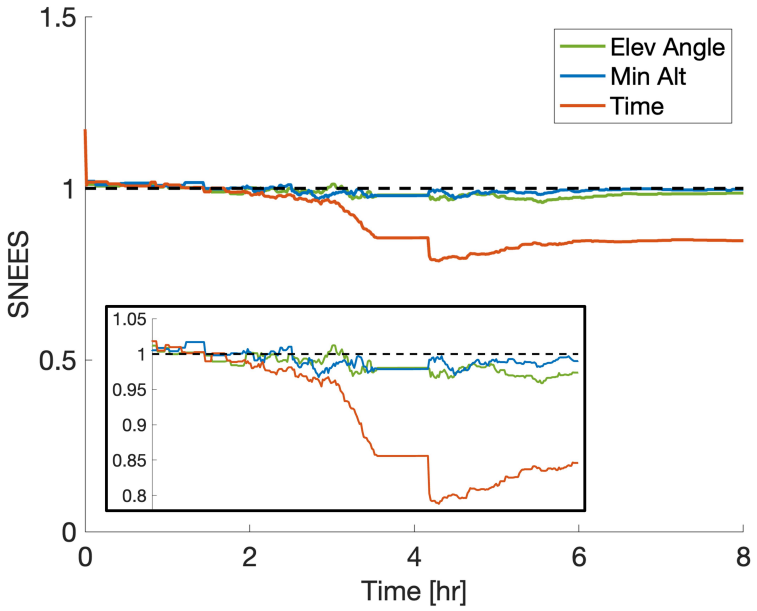


Fig. 7 SNEES over time for each measurement model.

$$\text{RMSE}_k = \sqrt{\frac{1}{N}\sum_{i=1}^{N}\left[\left(\eta_{x_k^{(i)}}\right)^2 + \left(\eta_{y_k^{(i)}}\right)^2 + \left(\eta_{z_k^{(i)}}\right)^2\right]} \tag{56}$$

at time t_k where, for example,

$$\eta_{x_k^{(i)}} = \hat{x}_k^{(i)} - x_k. \tag{57}$$

Here, x, y, and z are the components of the position or velocity in the Earth-Moon synodic frame. Table 3 below shows the time-averaged RMSE in both position and velocity for each measurement model.

Model	**Time-Averaged RMSE in Position [km]**	**Time-Averaged RMSE in Velocity [m/s]**
Elevation Angle	2.858	0.1810
Minimum Altitude	2.891	0.1816
Time	2.834	0.1722

Table 3 Time-averaged RMSE values for all three measurement models.

The time-averaged RMSE values being on the order of kilometers and centimeters per second for position and velocity, respectively, in Table 3 is indicative of an accurate state estimate. While theoretically the smallest possible RMSE is desired, all

three measurement models here have similar time-averaged RMSE values. Thus, for this well-behaving cislunar orbit determination scenario, both the RMSE and SNEES indicate that all three measurement models are effective for this problem.

6 Comparison of Measurement Models

It is of interest to assess the relative strengths of the three measurement models by examining other metrics, orbits, or edge cases. Specifically, measure of nonlinearity (MoNL) and measure of non-Gaussianity (MoNG) metrics are used here to differentiate between the occultation measurement models.

6.1 Measure of Nonlinearity

To isolate the measurement function itself, a mean squared error (MSE) MoNL is used to evaluate the nonlinearity of each measurement function [35]. The MSE MoNL, ν_{MSE}, is defined as

$$\nu_{\text{MSE}} = \sqrt{\frac{\text{tr}(P_{zz} - \boldsymbol{P}_{zx}\boldsymbol{P}^{-1}\boldsymbol{P}_{zx}^{T})}{\text{tr}(P_{zz})}} \tag{58}$$

where

$$P_{zz} = \boldsymbol{H}\bar{\boldsymbol{P}}\boldsymbol{H}^{T} + R, \qquad \boldsymbol{P}_{zx} = \boldsymbol{H}\bar{\boldsymbol{P}}, \tag{59}$$

and $\boldsymbol{P}$ is the estimated state covariance. This metric is inherently normalized because of the term in the denominator. It is also unit-invariant in this case because occultations produce scalar measurements. In this context, unit-invariant means that the units of the measurements do not affect the MoNL value. Additionally, while the trace operators in Eq. (58) are included for generality, they are redundant for the scalar measurements considered here.

Figure 8 shows the measure of nonlinearity as a function of time for each measurement model. Focusing on the averaged values, the time-based approach results in a more nonlinear measurement function than the other two approaches, which have similar values. As a result, the minimum altitude or elevation angle models may be more advantageous in specific scenarios because they remain closer to the linear regime.

6.2 Measure of Non-Gaussianity

In addition to the measurement function, the Gaussianity of the measurement error can also be analyzed. The primary source of measurement error is the camera detection error, w_{cam}, which is fundamentally a pixel-based error. This error is then mapped to an angular error using only camera parameters. While the angular error is additive for the elevation angle approach, it becomes state dependent for the other two approaches because of a nonlinear transformation. As a result, the measurement error may no longer satisfy the Gaussian assumption. To assess this, a skewness-based MoNG [35], defined as

$$\nu_{\mathrm{M3}} = \left| \sum_{i=1}^{N} \frac{(w_i - \bar{w})^3}{\sigma_w^3} \right|, \tag{60}$$

is used, where w_i is the transformed measurement error corresponding to the ith Monte Carlo iteration, $\bar{w}$ is the corresponding average, and σ_w is the corresponding standard deviation. The transformed measurement error, w, is defined as

$$w = G(\boldsymbol{r}) w_{\mathrm{cam}} \tag{61}$$

with $G(\boldsymbol{r})$ being the nonlinear transformation, where $G(\boldsymbol{r}) = 1$ for the elevation angle model.

To test the validity of the Gaussian assumption, an edge case is considered where the initial covariance is inflated to

$$\boldsymbol{P}_0 = \mathrm{diag}([\sigma_r, \sigma_r, \sigma_r, \sigma_v, \sigma_v, \sigma_v, 2.6 \times 10^{-7}]^2), \quad \sigma_r = 2 \times 10^{-3}, \quad \sigma_v = 1 \times 10^{-4}, \tag{62}$$

and no measurements are processed for the first hour. Due to the varying frequency of the occultation measurements, this setup could simulate a situation where there is poor observability of potential occultations, for example if the Moon is too bright. While large initial uncertainty values like these may be unrealistic in practice, the goal here is to accentuate the resulting non-Gaussianity of the measurement error for analysis purposes.

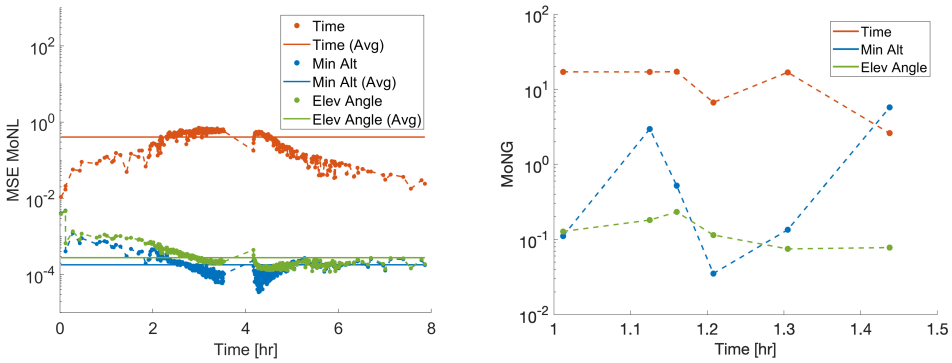


Fig. 8 MSE MoNL (left) for the full eight-hour trajectory and skewness-based MoNG (right) for a reduced interval.

Figure 8 shows the MoNG for the first half hour following the hour of no measurements. Higher MoNG values indicate that the camera detection error has become more skewed and non-Gaussian when mapped via Eq. (61). This is especially true for the time-based approach, but also for the minimum altitude model, which results in a sporadic temporal evolution of the non-Gaussianity. As expected though, only the elevation angle approach allows the measurement noise in the filter to remain consistently Gaussian and best reflect the intrinsic hardware error.

7 Future Work

Future work includes exploring additional scenarios where the nonlinearity of the time-based measurement or the non-Gaussianity of the camera detection error have a substantial effect on filter performance. This work may involve tuning various parameters or assessing the feasibility of occultations as a standalone measurement source for spacecraft in other orbits, including distant retrograde, Lissajous, and Lyapunov orbits. The full NRHO trajectory could also be used to understand how the measurement models perform in slower-moving regions of cislunar space. In cases where measurements become infrequent in these orbits, it would also be worthwhile examining the effectiveness of adding other measurement sources, such as apparent radius measurements, to complement the occultation measurements. Additionally, a digital elevation model (DEM) could be incorporated into both the truth and filter representations, replacing the conservative lunar radius error approach used here. Lastly, the fidelity could be further increased by modeling the attitude and pointing errors or constraints that are associated with keeping the dark lunar limb within the camera's FOV.

8 Conclusion

In general, star occultations provide position information without the need for an additional sensor. By repurposing an existing star tracker, the timing of occultations can be recorded and used as measurements onboard. Ideally, the occultations would then be processed using a time-based model to reflect the fundamental measurement form. However, the resulting measurement function is implicit, making it difficult to obtain a closed form algebraic expression. Thus, to process these measurements effectively, the implementation of the measurement model within the filter must be carefully considered.

In this paper, a new elevation angle approach for modeling star occultation measurements is proposed. Unlike the time-based approach, the elevation angle measurement function can be represented explicitly in closed form within the filter, similar to the minimum altitude model. In contrast to both existing approaches though, the new formulation allows the camera detection error to remain additive within the filter and better reflect the true hardware error characteristics. The effectiveness of all three measurement models was assessed using an EKF onboard a spacecraft in an Earth-Moon NRHO.

Analysis using the MoNL and MoNG metrics indicates that the elevation angle model both limits the nonlinearity of the measurement function and ensures that the camera detection error remains Gaussian. This angle-based mapping, as well as the distance-based approach, produces a consistent filter, whereas the time-based approach is slightly more conservative. While the time-averaged RMSE values indicate that each of the measurement approaches can yield accurate filters, the elevation angle model provides the most robustness across the various criteria. Overall, despite the measurement frequency being highly dependent on the dynamics, the performance near perilune demonstrates that star occultations can be an effective measurement source in the cislunar regime.

Declarations

Ethical Approval and Consent to Participate

Not applicable.

Human Ethics

Not applicable.

Consent for Publication

Not applicable.

Availability of Supporting Data

The supporting data is available from the corresponding author upon reasonable request.

Competing Interests

The authors have no competing interests to declare.

Funding

This research was funded in part by a NASA Space Technology Graduate Research Opportunity corresponding to grant number 80NSSC25K0236.

Authors' Contributions

Jack A. Joshi implemented the code, generated the results, and wrote the article. Renato Zanetti and Ryan P. Russell initiated and guided the research process. All authors reviewed the article.

Acknowledgements

This paper was presented at the Mortari Symposium to celebrate Dr. Mortari's influential career in spacecraft navigation, including star tracker data processing. The authors thank him for his feedback on this work itself. The authors would also like to acknowledge Matthew Gualdoni for his valuable insights into the relevance and applicability of star occultation measurements and for reviewing the paper.

Clinical Trial Registration and Number

Not applicable.

Appendix A Partial Derivatives of Approximated Time Measurement

The partials of the approximated time measurement are derived here to ensure filter consistency. The exact measurement partials with respect to the spacecraft's position, $\boldsymbol{H}_r$, and velocity, $\boldsymbol{H}_v$, are

$$\boldsymbol{H}_r = \frac{\partial t}{\partial \boldsymbol{r}} = \frac{1}{\boldsymbol{v}_r \cdot \boldsymbol{i}_p} \boldsymbol{i}_p^T \quad \text{and} \quad \boldsymbol{H}_v = \frac{\partial t}{\partial \boldsymbol{v}} = \boldsymbol{0}^T, \tag{A1}$$

based on the derivation from Battin [9], and will be leveraged later on. To begin, the partials of the predicted occultation time, from Eq. (19), with respect to position are

$$\frac{\partial \bar{t}}{\partial \bar{\boldsymbol{r}}} \approx \frac{\partial}{\partial \bar{\boldsymbol{r}}} \left(t - \frac{\bar{\varepsilon}}{\dot{\bar{\varepsilon}}} \right) = -\frac{\partial}{\partial \bar{\boldsymbol{r}}} \left(\frac{\bar{\varepsilon}}{\dot{\bar{\varepsilon}}} \right) = \frac{-1}{\dot{\bar{\varepsilon}}} \frac{\partial \bar{\varepsilon}}{\partial \bar{\boldsymbol{r}}} - \bar{\varepsilon} \frac{\partial}{\partial \bar{\boldsymbol{r}}} \left(\frac{1}{\dot{\bar{\varepsilon}}} \right). \tag{A2}$$

Going forward, the $\bar{(\cdot)}$ is dropped for conciseness, but the parameters are all evaluated at the predicted state. The first term in the expanded portion of Eq. (A2) becomes

$$-\frac{1}{\dot{\varepsilon}} \frac{\partial \varepsilon}{\partial \boldsymbol{r}} = -\frac{\partial t}{\partial \varepsilon} \frac{\partial \varepsilon}{\partial \boldsymbol{r}} = -\frac{\partial t}{\partial \boldsymbol{r}} = -\frac{1}{\boldsymbol{v}_r \cdot \boldsymbol{i}_p} \boldsymbol{i}_p^T, \tag{A3}$$

and the second term can be rewritten as

$$-\varepsilon \frac{\partial}{\partial \boldsymbol{r}} \left(\frac{1}{\dot{\varepsilon}} \right) = -\varepsilon \frac{\partial}{\partial \boldsymbol{r}} \left(\frac{\partial t}{\partial \varepsilon} \right) = -\varepsilon \frac{\partial}{\partial \boldsymbol{r}} \left(\frac{\partial \varepsilon}{\partial t} \right)^{-1}. \tag{A4}$$

Focusing on the partial derivative of the expression in Eq. (A4) results in

$$\begin{aligned} -\frac{\partial}{\partial \boldsymbol{r}} \left(\frac{\partial \varepsilon}{\partial t} \right)^{-1} &= \left(\frac{\partial \varepsilon}{\partial t} \right)^{-2} \frac{\partial}{\partial \boldsymbol{r}} \left(\frac{\partial \varepsilon}{\partial t} \right) = \dots \\ \dots &= \left(\frac{\partial \varepsilon}{\partial t} \right)^{-2} \frac{\partial}{\partial \boldsymbol{r}} \left(\frac{\partial \boldsymbol{r}^T}{\partial t} \frac{\partial \varepsilon}{\partial \boldsymbol{r}^T} \right) = \left(\frac{1}{\dot{\varepsilon}^2} \right) \boldsymbol{v}_r^T \frac{\partial^2 \varepsilon}{\partial \boldsymbol{r} \partial \boldsymbol{r}^T}. \end{aligned} \tag{A5}$$

All of the parameters in Eq. (A5) above are known except for the Hessian of the elevation angle with respect to position, which can be expressed as

$$\frac{\partial^2 \varepsilon}{\partial \boldsymbol{r} \partial \boldsymbol{r}^T} = \frac{\partial}{\partial \boldsymbol{r}} \left(\frac{1}{r \cos \rho} \boldsymbol{i}_p \right) = \frac{\partial}{\partial \boldsymbol{r}} \left(\frac{1}{r} \boldsymbol{i}_n + \tan \rho \, \boldsymbol{i}_r \right) \tag{A6}$$

with

$$\boldsymbol{i}_n = \frac{1}{\tan(\varepsilon + \rho)} \boldsymbol{i}_r + \frac{1}{\sin(\varepsilon + \rho)} \boldsymbol{i}_s, \tag{A7}$$

where $\boldsymbol{i}_s$, $\boldsymbol{i}_r$, and $\boldsymbol{i}_n$ are defined by Battin [9]. This can then be expanded using the chain rule, a few trigonometric identities, and the assumption that $\boldsymbol{i}_s$ does not depend on the state, since the star is sufficiently far away. This results in

$$\frac{\partial^2 \varepsilon}{\partial \boldsymbol{r} \partial \boldsymbol{r}^T} = \frac{1}{r} \left[-\frac{\boldsymbol{i}_n \boldsymbol{i}_r^T}{r} + \frac{\tan \rho (I - 2 \boldsymbol{i}_r \boldsymbol{i}_r^T)}{r} + \frac{\partial \boldsymbol{i}_n}{\partial \boldsymbol{r}} + \boldsymbol{i}_r \frac{\partial \tan \rho}{\partial \boldsymbol{r}} \right] \tag{A8}$$

where

$$\frac{\partial \boldsymbol{i}_n}{\partial \boldsymbol{r}} = -\csc(\varepsilon+\rho)[\csc(\varepsilon+\rho)\boldsymbol{i}_r + \cot(\varepsilon+\rho)\boldsymbol{i}_s]\left(\frac{\partial \varepsilon}{\partial \boldsymbol{r}} + \frac{\partial \rho}{\partial \boldsymbol{r}}\right) + \frac{I - \boldsymbol{i}_r \boldsymbol{i}_r^T}{r\tan(\varepsilon+\rho)}, \tag{A9}$$

$$\frac{\partial \tan\rho}{\partial \boldsymbol{r}} = \left(\frac{r^2}{r^2 - a_M^2}\right)\frac{\partial \rho}{\partial \boldsymbol{r}}, \tag{A10}$$

and

$$\frac{\partial \rho}{\partial \boldsymbol{r}} = -\frac{\tan\rho}{r}\,\boldsymbol{i}_r^T. \tag{A11}$$

To recap, the partials of the approximated occultation time measurement with respect to position, $\boldsymbol{H}_r^*$, are

$$\boldsymbol{H}_r^* = -\frac{1}{\boldsymbol{v}_r \cdot \boldsymbol{i}_p}\boldsymbol{i}_p^T + \left(\frac{\varepsilon}{\dot{\varepsilon}^2}\right)\boldsymbol{v}_r^T \frac{\partial^2 \varepsilon}{\partial \boldsymbol{r}\partial \boldsymbol{r}^T} \tag{A12}$$

with the Hessian term provided in Eqs. (A8) - (A11).

The partials of the approximated occultation time measurement with respect to velocity are a bit simpler to derive. Beginning with Eq. (19) again leads to

$$\frac{\partial}{\partial \boldsymbol{v}_r}\left(t - \frac{\varepsilon}{\dot{\varepsilon}}\right) = -\varepsilon\frac{\partial}{\partial \boldsymbol{v}_r}\left(\frac{1}{\dot{\varepsilon}}\right) \tag{A13}$$

where

$$\dot{\varepsilon} = \frac{\boldsymbol{v}_r^T \boldsymbol{i}_p}{r\cos\rho}. \tag{A14}$$

Taking the partial derivative then provides the following closed-form solution,

$$\boldsymbol{H}_v^* = \frac{\varepsilon r\cos\rho}{(\boldsymbol{v}_r^T \boldsymbol{i}_p)^2}\,\boldsymbol{i}_p^T. \tag{A15}$$

Lastly, the partial derivative of the approximated time measurement with respect to the lunar radius bias can be derived. The general form is given by

$$\frac{\partial}{\partial b}\left(t - \frac{\varepsilon}{\dot{\varepsilon}}\right) = -\frac{1}{\dot{\varepsilon}}\frac{\partial \varepsilon}{\partial b} - \varepsilon\frac{\partial}{\partial b}\left(\frac{1}{\dot{\varepsilon}}\right) \tag{A16}$$

where the first term becomes

$$-\frac{1}{\dot{\varepsilon}}\frac{\partial \varepsilon}{\partial b} = \frac{1}{\dot{\varepsilon}}\frac{\partial \rho}{\partial b} = \frac{1}{\dot{\varepsilon}}\frac{\partial}{\partial b}\left(\arcsin\left(\frac{R_{\text{☽}}}{r}\right)\right) = \frac{1}{\dot{\varepsilon}\sqrt{r^2 - R_{\text{☽}}^2}} \tag{A17}$$

with $R_{\text{☽}} = R_{\text{☽},avg} + b$. The second term is then

$$-\varepsilon\frac{\partial}{\partial b}\left(\frac{1}{\dot{\varepsilon}}\right) = -\varepsilon\frac{\partial}{\partial b}\left(\frac{r\cos\rho}{\boldsymbol{v}_r^T \boldsymbol{i}_p}\right) \approx -\frac{\varepsilon R_{\text{☽}}}{\boldsymbol{v}_r^T \boldsymbol{i}_p\sqrt{r^2 - R_{\text{☽}}^2}} \tag{A18}$$

where the dependence of $\boldsymbol{i}_p$ on ρ is considered to be negligible. Under that assumption, the measurement partials can be written as

$$H_b^* \approx \frac{1}{\dot{\varepsilon}\sqrt{r^2 - R_{\mathbb{D}}^2}} - \frac{\varepsilon R_{\mathbb{D}}}{\boldsymbol{v}_r^T \boldsymbol{i}_p \sqrt{r^2 - R_{\mathbb{D}}^2}}. \tag{A19}$$

Appendix B Comprehensive Set of Initial Conditions and Relevant Parameters

To allow for reproducibility of the results presented in this thesis, a comprehensive list of the initial conditions, fixed error parameters, and miscellaneous simulation values are included in Tables B1-B6 below.

Table B1 Initial true state and uncertainty.

Parameter	Symbol	Value	Units
Position	$\boldsymbol{r}_0$	[0.990736, -0.0223382, -0.0287614]	n.d.
Velocity	$\boldsymbol{v}_0$	[-0.0645360, 0.1952886, 0.7177936]	n.d.
Lunar radius bias	b_0	0	n.d.
1σ position error	$\sigma_{r,0}$	2.5×10^{-5}	n.d.
1σ velocity error	$\sigma_{v,0}$	1×10^{-4}	n.d.
1σ lunar radius bias error	$\sigma_{b,0}$	2.6×10^{-7}	n.d.

Table B2 Other modeling and measurement error sources.

Parameter	Symbol	Value	Units
Camera detection error	σ_{cam}	0.5	pixel
Time-tag uncertainty	σ_{time}	$\Delta t_{\text{cam}}/\sqrt{12}$	s
Camera frame rate	$\Delta t_{\text{cam}}^{-1}$	1	Hz

Table B3 General simulation parameters.

Parameter	Symbol	Value	Units
Time step	Δt	1	s
Duration	$t_f - t_0$	8	hr
Monte Carlo iterations	N	1000	–

Table B4 CR3BP parameters.

Parameter	Symbol	Value	Units
Earth's gravitational parameter	$\mu_{\oplus}$	3.986×10^{14}	m^3/s^2
Moon's gravitational parameter	$\mu_{\mathfrak{D}}$	4.902×10^{12}	m^3/s^2
Characteristic length	l^*	384400	km
Characteristic time	t^*	$\sqrt{(l^*)^3/[G(m_{\oplus} + m_{\mathfrak{D}})]}$	s

Table B5 Measurement parameters.

Parameter	Symbol	Value	Units
Number of stars	n_*	4995	–
Average lunar radius	$R_{\mathfrak{D},\max}$	1737.5	km
Camera field of view	FOV	20	deg
Number of pixels	n_{pixel}	1024	–
Maximum Moon illumination	$k_{\mathfrak{D},\max}$	80	%

Table B6 Miscellaneous parameters.

Parameter	Symbol	Value	Units
True radius bias correlation distance	δ	50	m
Onboard radius bias time constant	τ	1×10^{10}	min
Right ascension of Sun	$\alpha_{\odot}$	153.2597	deg
Declination of Sun	$\delta_{\odot}$	56.6251	deg

References

[1] Karimi, R.R., Mortari, D.: Interplanetary autonomous navigation using visible planets. Journal of Guidance, Control, and Dynamics **38**(6), 1151–1156 (2015) https://doi.org/10.2514/1.G000575

[2] Mortari, D., Conway, D.: Single-point position estimation in interplanetary trajectories using star trackers. Celestial Mechanics and Dynamical Astronomy **128**, 115–130 (2017) https://doi.org/10.1007/s10569-016-9738-4

[3] Kobylka, K.R.: Photometric and geometric methods for enhanced image-based spacecraft navigation. PhD thesis, Rensselaer Polytechnic Institute (2021). https://www.proquest.com/dissertations-theses/photometric-geometric-methods-enhanced-image/docview/2727668983/se-2

[4] Navqi, A.M.: Satellite navigation by terrestrial occultations of stars I: General considerations neglecting atmospheric refraction and extinction. Technical Report 62-18-A, Geophysics Corporation of America (1962). https://apps.dtic.mil/sti/tr/pdf/AD0287867.pdf

[5] Keenan, R.V., Regenhardt, J.D.: Star occultation measurements as an aid to navigation in cis-lunar space. Master's thesis, Massachusetts Institute of Technology (1962). http://hdl.handle.net/1721.1/38738

[6] Lillestrand, R.L., Carroll, J.E.: Horizon-based satellite navigation systems. IEEE Transactions on Aerospace and Navigational Electronics **10**(3), 247–270 (1963) https://doi.org/10.1109/TANE.1963.4502122

[7] Lillestrand, R.L., Carroll, J.E.: Dynamic Space Navigation Employing Star Occultation Technique. U.S. Patent 3,360,638 (1967). https://ppubs.uspto.gov/basic/

[8] Zeitler, E.O., Rogers, T.G.: The Gemini program: Physical sciences experiments summary. Technical Report NASA-TM-X-58075, NASA (1971). https://ntrs.nasa.gov/api/citations/19720003207/downloads/19720003207.pdf

[9] Battin, R.H.: An Introduction to the Mathematics and Methods of Astrodynamics, Revised edn., pp. 628–630. American Institute of Aeronautics and Astronautics, Reston, VA (1999). Chap. 13. https://doi.org/10.2514/4.861543

[10] Psiaki, M.L., Hinks, J.C.: Autonomous Lunar Orbit Determination Using Star Occultation Measurements. In: AIAA Guidance, Navigation and Control Conference and Exhibit (2007). AIAA 2007-6657. https://doi.org/10.2514/6.2007-6657

[11] Crouse, B.: Autonomous optical navigation for lunar missions. Master's thesis, Rice University (2009). https://hdl.handle.net/1911/61858

[12] Maybeck, P.S.: Stochastic Models, Estimation, and Control vol. 1. Academic Press (1979). https://www.sciencedirect.com/bookseries/mathematics-in-science-and-engineering/vol/141/part/P1

[13] Howell, K.C., Breakwell, J.V.: Almost rectilinear halo orbits. Celestial Mechanics **32**(1), 29–52 (1984) https://doi.org/10.1007/BF01358402

[14] Williams, J., Lee, D.E., Whitley, R.J., Bokelmann, K.A., Davis, D.C., Berry, C.F.: Targeting cislunar near rectilinear halo orbits for human space exploration. In: 27th AAS/AIAA Space Flight Mechanics Meeting (2017). AAS 17-267. https://ntrs.nasa.gov/api/citations/20170001352/downloads/20170001352.pdf

[15] Low, L.E.: NASA Unveils Initiatives to Achieve America's National Space Policy (2026). https://www.nasa.gov/news-release/nasa-unveils-initiatives-to-achieve-americas-national-space-policy/

[16] Zanetti, R.: Autonomous midcourse navigation for lunar return. Journal of Spacecraft and Rockets **46**(4), 865–873 (2009) https://doi.org/10.2514/1.41769

[17] Carpenter, J.R., D'Souza, C.N.: Navigation filter best practices (revised). Technical Report TP–2018–219822, NASA (2025). https://ntrs.nasa.gov/api/citations/20250002787/downloads/20250002787.pdf

[18] Gadeberg, B.L., White, K.C.: Theory of the correction of celestial observations made for spacecraft navigation or training. Technical Report NASA TN D-5239, NASA Ames Research Center (1970). https://ntrs.nasa.gov/api/citations/19700008007/downloads/19700008007.pdf

[19] Spreen, E.M.Z.: Trajectory design and targeting for applications to the exploration program in cislunar space. PhD thesis, Purdue University (2021). https://doi.org/10.25394/PGS.14445717

[20] Newman, C.P., Ott, C., Aguilar, A., Davis, D.C.: Navigation Performance Overview of Gateway During a Lunar Lander Mission. In: 2024 AAS/AIAA Astrodynamics Specialist Conference (2024). AAS 24-355. https://ntrs.nasa.gov/api/citations/20240008729/downloads/NRHO_OD_4_final_final.pdf

[21] Getchius, J., D'Souza, C., Crain, T.: Optical Navigation for the Orion Vehicle. In: 18th AAS/AIAA Space Flight Mechanics Meeting (2008). https://ntrs.nasa.gov/api/citations/20080009587/downloads/20080009587.pdf

[22] Christian, J.A.: Optical navigation using planet's centroid and apparent diameter in image. Journal of Guidance, Control, and Dynamics **38**(2), 192–204 (2015) https://doi.org/10.2514/1.G000872

[23] Brown, G.M., Peterson, L.T., Henry, D.B., Scheeres, D.J.: Behavior of symmetric periodic orbits with high-order resonance in the sun-earth-moon system. The Journal of Astronautical Sciences **72**(43) (2025) https://doi.org/10.1007/s40295-025-00517-3

[24] Perryman, M.A.C., *et al.*: The Hipparcos Catalogue. Astronomy and Astrophysics **323**, 49–52 (1997). https://articles.adsabs.harvard.edu/pdf/1997A%26A...323L..49P

[25] Jena-Optronik GmbH: Autonomous Star Sensor ASTRO APS. (2015). https://jena-optronik.de/products/star-sensors/star-sensor-astro-15.html

[26] Kalman, R.E.: A new approach to linear filtering and prediction problems. Transactions of the ASME-Journal of Basic Engineering **82**(1), 35–45 (1960) https://doi.org/10.1115/1.3662552

[27] Kalman, R.E., Bucy, R.S.: New results in linear filtering and prediction theory. Transactions of the ASME-Journal of Basic Engineering **83**(1), 95–108 (1961)

https://doi.org/10.1115/1.3658902

[28] Tapley, B.D., Schutz, B.E., Born, G.H.: Statistical Orbit Determination, pp. 209–211. Elsevier (2004). Chap. 4. https://doi.org/10.1016/B978-0-12-683630-1.X5019-X

[29] Brouk, J.D., DeMars, K.J.: Kalman filtering with uncertain and asynchronous measurement epochs. NAVIGATION: Journal of the Institute of Navigation **71**(3) (2024) https://doi.org/10.33012/navi.652

[30] Schmidt, S.F.: Application of state-space methods to navigation problems. Advances in Control Systems, vol. 3, pp. 293–340. Elsevier (1966). https://doi.org/10.1016/B978-1-4831-6716-9.50011-4

[31] Boone, S., Boodram, O., McMahon, J.: Efficient Nonlinear Filtering Methods for Near-Rectilinear Halo Orbit Navigation. In: 2023 AAS GN&C Conference (2023). AAS 23-065. https://ntrs.nasa.gov/api/citations/20240008729/downloads/NRHO_OD_4_final_final.pdf

[32] Barker, M.K., Mazarico, E., Neumann, G.A., Smith, D.E., Zuber, M.T., Head, J.W.: Improved LOLA elevation maps for south pole landing sites: Error estimates and their impact on illumination conditions. Planetary and Space Science **203** (2021) https://doi.org/10.1016/j.pss.2020.105119

[33] Christian, J.A.: Fundamentals of Spacecraft Optical Navigation. John Wiley & Sons (2026). https://doi.org/10.1002/9781394267743

[34] Bar-Shalom, Y., Li, X.R., Kirubarajan, T.: Estimation with Applications to Tracking and Navigation: Theory Algorithms and Software, pp. 234–235. John Wiley & Sons (2001). Chap. 5. https://doi.org/10.1002/0471221279

[35] Havlík, J., Straka, O.: Measures of Nonlinearity and Non-Gaussianity in Orbital Uncertainty Propagation. In: 22nd International Conference on Information Fusion (2019). https://doi.org/10.23919/FUSION43075.2019.9011445